

3 **A vorticity budget for theoretical and**  
4 **convectively-coupled equatorial Rossby waves:**  
5 **Dynamical propagation and growth mechanisms**

6 **Adrian J. Matthews<sup>1</sup>**

<sup>1</sup>Centre for Ocean and Atmospheric  
7 Sciences, School of Environmental Sciences  
and School of Mathematics, University of  
East Anglia, Norwich, United Kingdom

Convectively coupled equatorial Rossby waves (CCERWs)

**Correspondence**

Prof. Adrian Matthews, School of  
Environmental Sciences, University of East  
Anglia, Norwich, United Kingdom  
Email: a.j.matthews@uea.ac.uk

**Funding information**

Natural Environment Research Council  
through the TerraMaris project (grant  
NE/R016704/1).

are westward-propagating tropical weather systems, that can trigger extreme precipitation and flooding. Here, vorticity budgets are used to determine their dynamical mechanisms of propagation and growth. First, an analytical solution to the vorticity budget of theoretical dry  $n = 1$  equatorial Rossby waves is presented. Westward propagation arises entirely from the planetary vorticity advection ( $-\beta v$ ) term, where high magnitude planetary vorticity is advected equatorward from higher latitudes to the west of cyclonic perturbations in the Rossby wave structure. This is the classical Rossby wave propagation mechanism. There is one other non-zero term in the vorticity budget; the vortex stretching ( $-fD$ ) term has a (weak) eastward propagation tendency, mainly due to the convergence in the meridional wind structure to the east of the cyclonic perturbations. This acts to slow the overall westward propagation down. Both these terms are in quadrature with the vorticity structure, and hence the theoretical waves are neutral.

A vorticity budget of observed CCERWs is then presented, using reanalysis data. The primary westward propagation mechanism is still the planetary vorticity advection term. However, the convergence centres are now aligned with the cyclonic vorticity centres, rather than a quarter cycle to the east. Hence the vortex stretching ( $-fD$ ) term is now in phase with the vorticity, leading to growth of the CCERWs. There is an even stronger growth contribution from the non-linear vortex stretching  $-\zeta D$  term. Horizontal vorticity advection and sub grid scale processes both act to damp the CCERW. The total source term is one of westward propagation and growth. This diagnostic vorticity budget approach can be applied to inform the assessment of forecast skill and model development.

#### KEYWORDS

equatorial Rossby wave, convection, vorticity budget, propagation mechanism, growth mechanism

## 9 1 | INTRODUCTION

10 Convectively coupled equatorial Rossby waves (CCERWs) are westward-propagating tropical weather systems that  
11 are found ubiquitously in the major tropical convective regions (Takayabu, 1994; Wheeler and Kiladis, 1999). They  
12 have a coherent precipitation and dynamical structure associated with them (Wheeler et al., 2000; Yang et al., 2003).  
13 CCERWs have a relatively slow propagation speed, such that the local precipitation signal can last over one week in  
14 a given location. Hence they are a major contributor to precipitation variability on subseasonal time scales (Tsai et al.,  
15 2020) and an important source of subseasonal prediction skill (Dias et al., 2023). In particular, they are important  
16 components of the subseasonal variability in the major monsoon systems over West Africa (Janicot et al., 2010) and  
17 South Asia through the Boreal Summer Intraseasonal Oscillation (Kemball-Cook and Wang, 2001).

18 Recently, there has been a surge of interest in the role of CCERWs, and convectively coupled equatorial waves  
19 in general, on extreme precipitation (Baranowski et al., 2020). This is based on the multi-scale interaction structure  
20 of convective systems in the tropics, where the slowly varying, large-scale structures (such as CCERWs) set the envi-  
21 ronment within which shorter time scale, smaller spatial scale structures (such as mesoscale convective systems) can  
22 develop and produce local extreme precipitation (Meehl et al., 2001). For example, the probability of extreme precip-  
23 itation increases by a factor of three over eastern Malaysia and the Philippines during the passage of the envelope of  
24 convection associated with CCERWs during the northern winter season (Ferrett et al., 2020).

25 Additionally, CCERWs can also interact non-linearly with other tropical weather system. For example, the proba-  
26 bility of extreme precipitation and/or flooding in Sulawesi doubles if either a CCERW or a convectively coupled Kelvin  
27 wave (CCKW) is present (Latos et al., 2021). If both occur simultaneously, the probability increases by a factor of eight.  
28 As well as increasing the probability of extreme precipitation within the large-scale convective envelope, CCERWs can  
29 also indirectly contribute to extreme precipitation. During the development of Tropical Cyclone Seroja, a moisture sup-  
30 ply was provided by a CCERW that advected moist air around its lower tropospheric cyclonic part to feed into the  
31 developing tropical cyclone (Latos et al., 2023). In a similar manner, CCERWs have also been linked to cold surges  
32 on the western flank of their cyclonic anomalies over the South China Sea, leading to extreme precipitation there  
33 (Diong et al., 2023). In general, CCERWs have a well established link with tropical cyclone genesis (Frank and Roundy,  
34 2006); globally, 60% of pre-tropical cyclogenesis events are associated with CCERW precursors (Feng et al., 2023).  
35 The causal mechanism here appears to be an increase in mid-level relative humidity and low-level cyclonic vorticity  
36 associated with the CCERW (Zhao and Wu, 2018).

37 From their inception in the 1990s, CCERWs have been implicitly assumed to be essentially analogues of the  
38 westward-propagating theoretical dry equatorial Rossby waves (Matsuno, 1966), modified by moist convection (Ki-  
39 ladis et al., 2009). Similarly, the other classes of theoretical equatorial waves (Kelvin, mixed Rossby-gravity, inertio-  
40 gravity) also have their convectively coupled equatorial wave (CCEW) analogues. This assumption is also made in prac-  
41 tice, as the two main methods of diagnosing CCEWs in general (Knippertz et al., 2022) use this: 1) The wavenumber-  
42 frequency filtering method is based on the dispersion curves of the theoretical equatorial waves (Wheeler and Kiladis,  
43 1999); 2) The dynamical structure method is based on projecting wind data onto the meridional dynamical structure  
44 of the theoretical waves (Yang et al., 2003). The success of both of these methods justifies that assumption.

45 As implicit in the name, coupling with convection is key to understanding the mechanisms of CCERWs. Convection  
46 within CCERWs is observed to be in phase with the total column water anomaly, and convection in their active region  
47 is actually due to triggering of mesoscale interactions (Nakamura and Takayabu, 2022b). Fuchs-Stone et al. (2019)  
48 postulated that CCERWs are unstable moisture modes, using the Wind-Induced Surface Heat Exchange (WISHE)  
49 framework. The phase speed of an initial westward-propagating free equatorial Rossby wave slowed down when  
50 the wave was coupled with convection, due to WISHE and cloud-radiation interactions. Background easterly shear

51 can also help to destabilise such a westward propagating moisture mode (Chen, 2022). The interaction between  
 52 convection and dynamics and the related thermodynamical mechanisms are crucial to understand the propagation  
 53 and growth of convectively coupled equatorial waves, including CCERWs.

54 However, insights can also be gained by examining the purely dynamical balances within such waves. Such an  
 55 analysis was recently carried out for CCKWs (Matthews, 2021). Here, a vorticity budget analysis was performed for  
 56 both theoretical equatorial Kelvin waves and observed CCKWs. The dynamical eastward propagation of the CCKW  
 57 could be accounted for, as a modified version of the vorticity balance within the theoretical Kelvin wave. Hence,  
 58 although the overall general structure of CCERWs has been well documented, their vorticity and related divergence  
 59 structures are not well known.

60 The purpose of this paper is to establish the dynamical mechanisms of the propagation and growth of observed  
 61 CCERWs and to compare them to those same mechanisms in the theoretical equatorial Rossby waves. It is intended  
 62 as a follow on paper to Matthews (2021). The main hypothesis to be tested is that the CCERW acts dynamically like  
 63 a modified dry equatorial Rossby wave. It is anticipated that the main westward propagation mechanism will still be  
 64 the standard Rossby wave mechanism of meridional advection of planetary vorticity, but that this will be modified  
 65 by the addition of other vorticity source terms. A further hypothesis is that there will be vorticity source terms that  
 66 will enable the CCERW to grow, in contrast to theoretical equatorial Rossby waves which are neutral waves with zero  
 67 growth.

68 The study region will be the Indian Ocean. CCERWs occur throughout the tropics, but the Indian Ocean is a  
 69 large, mainly homogeneous ocean basin, where convection can occur over a wide range of tropical latitudes. All other  
 70 tropical regions will introduce confounding factors that may mask the propagation and growth regions of CCERWs.  
 71 Over Africa and South America, land-atmosphere interactions and moisture availability will likely be a complicating  
 72 factor. Over the Maritime Continent, the complex geometry of the large islands and shallow seas will also add a layer  
 73 of complexity. The Pacific Ocean is also a large ocean basin, but convection is limited over much of it to a narrow  
 74 Intertropical Convergence Zone (ITCZ) to the north of the equator, restricting convection to a limited latitude domain  
 75 and complicating analysis of the underlying mechanisms. Finally, the Atlantic also suffers from the ITCZ problem, and  
 76 is also relatively longitudinally narrow.

## 77 2 | THEORETICAL LINEAR EQUATORIAL ROSSBY WAVE

78 In Section 2.1, the structure of theoretical equatorial Rossby waves is summarised, following, e.g., Matsuno (1966)  
 79 and Gill (1982). This is followed in Section 2.2 by an analysis of the dynamical propagation and growth mechanisms  
 80 of these theoretical equatorial Rossby waves using a vorticity budget approach, following Matthews (2021).

### 81 2.1 | Equatorial Rossby wave dynamical structure

82 The equations of motion are linearised about a background atmosphere of zero motion, leading to a separation of  
 83 variables into two systems: 1) a vertical structure equation giving the vertical structure (e.g., first internal mode),  
 84 and 2) the shallow water equations governing the horizontal and time structure. The shallow water equations on an  
 85 equatorial beta plane ( $f = \beta y$ ), with zonal wind speed  $u(x, y, t)$ , meridional wind speed  $v(x, y, t)$ , geopotential height  
 86  $Z(x, y, t)$  are:

$$\frac{\partial u}{\partial t} - \beta y v = -g \frac{\partial Z}{\partial x}; \quad \frac{\partial v}{\partial t} + \beta y u = -g \frac{\partial Z}{\partial y}; \quad g \frac{\partial Z}{\partial t} + c_e^2 \left( \frac{\partial u}{\partial x} + \frac{\partial v}{\partial y} \right) = 0. \quad (1)$$

87 Here,  $x$  is distance eastward,  $y$  is distance northward from the equator,  $t$  is time,  $\beta = 2.3 \times 10^{-11} \text{ m}^{-1} \text{ s}^{-1}$  is the  
 88 northward gradient of planetary vorticity,  $g = 9.81 \text{ m s}^{-2}$  is the acceleration due to gravity, and  $c_e$  is the gravity wave  
 89 speed of the solutions and is related to the separation constant at the separation of variables step above.

90 The solutions can be separated further, in the form:

$$u(x, y, t) = \hat{u}(y)e^{i(kx-\omega t)}; \quad v(x, y, t) = \hat{v}(y)e^{i(kx-\omega t)}; \quad Z(x, y, t) = \hat{Z}(y)e^{i(kx-\omega t)}, \quad (2)$$

91 where the  $\hat{u}$ ,  $\hat{v}$  and  $\hat{Z}$  variables contain the (unknown)  $y$  structures of the solutions, and the  $x$  and  $t$  structures are  
 92 combined into a travelling wave with wavenumber  $k$  in the  $x$  direction, and frequency  $\omega$ . A single ordinary differential  
 93 equation can then be obtained for  $\hat{v}$ . The solutions are parabolic cylinder functions, and the dispersion relation is

$$\frac{c_e}{\beta} \left( \frac{\omega^2}{c_e^2} - k^2 - \frac{\beta k}{\omega} \right) = 2n + 1, \quad (3)$$

94 where  $n$  is any positive integer. The solution for the physically important  $n = 1$  equatorial Rossby wave is

$$\hat{v}(y) = 2v_0 \left( \frac{\beta}{c_e} \right)^{1/2} y e^{-\beta y^2 / 2c_e}, \quad (4)$$

95 where  $v_0$  is an arbitrary amplitude parameter, with dimensions of speed.

96 Solutions to  $\hat{u}(y)$  and  $\hat{Z}(y)$  are assumed to have the form:

$$\hat{u}(y) = u^*(y)e^{-\beta y^2 / 2c_e}; \quad \hat{Z}(y) = Z^*(y)e^{-\beta y^2 / 2c_e}. \quad (5)$$

97 The functions  $u^*$  and  $Z^*$  are then

$$u^*(y) = \frac{2iv_0 \left( \frac{\beta}{c_e} \right)^{1/2} [\beta(\omega + kc_e)y^2 - kc_e^2]}{(\omega^2 - k^2c_e^2)}, \quad (6)$$

98

$$Z^*(y) = \frac{\omega}{gk} u^*(y) - \frac{2\beta i}{gk} v_0 \left( \frac{\beta}{c_e} \right)^{1/2} y^2. \quad (7)$$

99 Note that where the imaginary number  $\pm i$  appears, it can be rewritten as  $e^{\pm i\tau/4}$ , with  $\tau = 2\pi$ . This can then be absorbed  
 100 into the complex exponential in the full solution to give  $e^{i(kx-\omega t \pm \tau/4)}$ , leading to a quarter cycle shift to the east (west)  
 101 in that part of the wave structure.

102 Rossby waves are low frequency, so the full dispersion relation can be approximated by neglecting the quadratic  
 103 term in Equation 3 to get the approximate ( $n = 1$ ) Rossby wave dispersion relation

$$\omega = -\frac{\beta k}{k^2 + 3\beta/c_e}. \quad (8)$$

104 Hence, for a given wavenumber  $k$ , the meridional wind  $v$  can be calculated from Equations 4 and 2. Using the fre-  
 105 quency  $\omega$  from Equation 8, the zonal wind  $u$  can then be calculated from Equations 6, 5 and 2. If desired, the geopo-  
 106 tential height  $Z$  can be calculated from Equations 7, 5 and 2. The relative vorticity  $\zeta$  and divergence  $D$  fields of the

107 equatorial Rossby wave are then calculated as:

$$\zeta = \frac{\partial v}{\partial x} - \frac{\partial u}{\partial y}, \quad D = \frac{\partial u}{\partial x} + \frac{\partial v}{\partial y}. \quad (9)$$

108 The theoretical structure of a sample  $n = 1$  equatorial Rossby wave is shown in Figure 1. This sample wave  
 109 has a zonal wavenumber of 7 (i.e., 7 complete wavelengths around the equator of an Earth-sized planet, such that  
 110  $k = 1.10 \times 10^{-6} \text{ m}^{-1}$ ), and the gravity wave speed was set to  $c_e = 12 \text{ m s}^{-1}$ . These arbitrary values of the zonal  
 111 wavenumber and gravity wave speed were chosen so as to produce a sample theoretical equatorial Rossby wave  
 112 whose spatial characteristics reasonably approximate those of the observed CCERWs presented later in Section 3.  
 113 From Equation 8, the (zonal) phase speed of this wave is  $c_x = \omega/k = -3.30 \text{ m s}^{-1}$ . This wave pattern can be considered  
 114 as representative of the lower tropospheric structure. When it is multiplied by the vertical structure calculated from  
 115 the vertical structure equation, e.g., the first internal mode (not shown), this leads to the same pattern but with  
 116 opposite sign in the upper troposphere.

117 The wave structure has a pair of cyclonic vorticity anomalies, centred at  $75^\circ\text{E}$ , with westerlies on the equator,  
 118 and easterlies off the equator to the north and south. Equatorward flow to the west and poleward flow to the east  
 119 completes the circulation around the cyclonic vorticity anomalies (anti-clockwise in the Northern Hemisphere and  
 120 clockwise in the Southern Hemisphere). The divergence field is symmetric about the equator, with convergence to  
 121 the east of the cyclonic anomalies and divergence to west. Convergence/divergence is actually a maximum off the  
 122 equator, at about  $8^\circ$  latitude for this example equatorial Rossby wave, with convergence in the poleward flow to  
 123 the east and divergence in the equatorward flow to the west, mainly from the  $\partial v/\partial y$  component. Hence, the initial  
 124 expectation might be that the precipitation structure of the observed CCERWs (to be presented in Section 3.2) would  
 125 follow the convergence structure of their theoretical counterpart, and therefore be found to the east of the twin lower  
 126 tropospheric cyclones, and be approximately symmetric about the equator, with off-equatorial maxima.

## 127 2.2 | Equatorial Rossby wave vorticity budget

128 The vorticity equation for the flow on a single pressure ( $p$ ) level can be written as

$$\frac{\partial \zeta}{\partial t} = \underbrace{-u \frac{\partial \zeta}{\partial x} - v \frac{\partial \zeta}{\partial y} - \omega \frac{\partial \zeta}{\partial p}}_{\text{advection of relative vorticity}} \quad \underbrace{-\zeta D - f D}_{\text{vortex stretching}} \quad (10)$$

$$\underbrace{-\beta v}_{\text{advection of planetary vorticity}} \quad \underbrace{-\left(\frac{\partial \omega}{\partial x} \frac{\partial v}{\partial p} - \frac{\partial \omega}{\partial y} \frac{\partial u}{\partial p}\right)}_{\text{tilting/twisting}}$$

129 where  $\omega$  is the vertical velocity in pressure coordinates. This leads to the concept of a vorticity budget, where the  
 130 vorticity tendency  $\partial \zeta/\partial t$  on the left is composed of the sum  $S$  of the vorticity source terms on the right. The vorticity  
 131 budget for the theoretical equatorial Rossby wave is presented in Figure 2. In each panel, the vorticity field of the  
 132 equatorial Rossby wave from Figure 1 is shown by the line contours, while the relevant vorticity source is colour  
 133 shaded.

134 The largest source term is advection of planetary vorticity  $-\beta v$  (Figure 2a). Focusing on the Northern Hemisphere

135 cyclone (positive vorticity anomaly) at  $75^\circ\text{E}$ , the equatorward flow to the west advects high planetary vorticity from  
136 the north, giving a positive vorticity tendency to the west. To the east, the poleward flow advects low planetary  
137 vorticity from the south, giving a negative vorticity tendency to the east. Hence, the vorticity source lies a quarter  
138 wavelength to the west of the vorticity anomaly and the net effect is to move the original cyclone (positive vorticity  
139 anomaly) westwards. This is the standard Rossby wave propagation mechanism.

140 There is also a contribution from the  $-fD$  vortex stretching term (Figure 2b). The convergence to the east of  
141 the cyclone (positive vorticity anomaly) leads to a positive vorticity tendency there. Similarly, the divergence to the  
142 west leads to a negative vorticity tendency. Hence, the  $-fD$  vortex stretching source lies a quarter wavelength to  
143 the east of the vorticity anomaly, and its effect is one of eastward propagation. All the other vorticity source terms in  
144 Equation 10 are nonlinear and are zero for the linear theoretical equatorial Rossby wave.

145 The advection of planetary vorticity term is larger in magnitude than the vortex stretching term, hence the total  
146 source term (Figure 2c) has a positive vorticity tendency to the west of the cyclone (positive vorticity anomaly) and a  
147 negative vorticity tendency to the east. Therefore, the total source leads to the expected westward propagation of  
148 the equatorial Rossby wave.

149 Note that the theoretical budget presented here is not perfect. The vorticity tendency  $\partial\zeta/\partial t$  (not shown) and the  
150 total vorticity source (Figure 2c) match each other very closely (their maps are visually indistinguishable). However,  
151 there is a small (2%) difference in amplitude. This arises from when the full dispersion relation (Equation 3) was  
152 approximated to the Rossby wave dispersion relation (Equation 8).

153 The  $-fD$  vortex stretching term effectively slows down the westward propagation speed of the equatorial Rossby  
154 wave. The westward tendency from the planetary vorticity advection term has a magnitude of approximately  $28 \times$   
155  $10^{-12} \text{ s}^{-2}$ , but the (westward) total source term has a magnitude of only  $21 \times 10^{-12} \text{ s}^{-2}$ . Hence if all other things were  
156 equal, the eastward tendency from the vortex stretching term “slows down” the westward propagation speed of the  
157 wave by about 25%.

158 However, all other things are not equal, as the latitudinal structures of the  $-\beta v$  and  $-fD$  source terms (Figure 2a,b)  
159 are not the same, and are not equal to the latitudinal structure of relative vorticity. However, when the two source  
160 terms are superimposed (Figure 2c), the total source term does have the same latitudinal structure as the relative  
161 vorticity. Hence, if the vortex stretching term was somehow removed, the remaining planetary vorticity advection  
162 term would not have the same latitudinal structure as the relative vorticity perturbation, and the wave would not  
163 propagate simply westward with no change of shape.

164 Hence, any changes to the structure of observed CCERWs from the theoretical structure of equatorial Rossby  
165 waves will likely have impacts on the magnitude of the westward phase speed and also on the coherent structure of  
166 the wave.

### 167 3 | OBSERVED CONVECTIVELY COUPLED EQUATORIAL ROSSBY WAVE

168 In this section, the structure of observed CCERWs is revisited, focusing on their vorticity and divergence structures.  
169 A vorticity balance of observed CCERWs is constructed, and compared with that of the theoretical equatorial Rossby  
170 waves.

### 171 3.1 | Data and methodology

172 The dynamical structure and vorticity budget for CCKWs were previously analysed by Matthews (2021). Here, that  
173 methodology is adapted for CCERWs. Full details of the methodology are in Matthews (2021); an outline is provided  
174 here.

175 The CCERW analysis is based on the gridded Integrated Multi-satellite Retrievals for GPM (IMERG) version 07B  
176 precipitation data set (Huffman et al., 2019). The IMERG data were retrieved from 1 July 2000 to 31 December 2023,  
177 on a 0.1 by 0.1 degree global latitude–longitude grid at 30 minute time resolution. They were regridded to a 0.25 by  
178 0.25 degree grid and 3-hourly means, for ease of computation.

179 The precipitation data were then latitudinally averaged from 15°S to 15°N, to effectively produce a Hovmöller  
180 time–longitude diagram of equatorial precipitation. Following Wheeler and Kiladis (1999), this Hovmöller diagram  
181 was then wavenumber–frequency filtered to extract the CCERW signals only; only westward-propagating waves  
182 lying between the dispersion curves of  $n = 1$  equatorial Rossby waves with equivalent depths of 2.5 m and 90 m,  
183 and with frequencies between  $1/60 \text{ day}^{-1}$  and  $1/2.5 \text{ day}^{-1}$ , and zonal wavenumbers between 1 and 10, were passed  
184 by the filter. Following Baranowski et al. (2016), CCERW trajectories were then defined to lie along the maxima in  
185 this Hovmöller diagram of CCERW wavenumber–frequency filtered precipitation. This leads to a full pan-tropical  
186 event-based data set of CCERW trajectories.

187 A base point was then defined, at 75°E in the central Indian Ocean for this study. A total of 208 CCERW trajec-  
188 tories crossed this base point during their life times, producing a set of 208 crossing times. Lagged composite means  
189 were constructed by averaging any variable of interest over those 208 crossing times. Hence, lag day 0 corresponds  
190 to the time of the CCERW crossing the base point at 75°E. Composites were initially constructed of the IMERGV07B  
191 precipitation itself, to identify the convective/precipitation signal associated with the CCERWs.

192 For dynamical variables (zonal and meridional wind components, horizontal divergence, relative vorticity), the  
193 ERA5 reanalysis data set was used (Hersbach et al., 2020). The ERA5 data were initially on a 0.25 by 0.25 degree grid  
194 with hourly time resolution. These were regridded to an approximately 0.7 by 0.7 degree grid and 3-hourly means,  
195 for ease of computation. Prior to compositing, the ERA5 data were also wavenumber–frequency filtered (separately  
196 at each latitude) for CCERW signals to increase the signal-to-noise ratio.

### 197 3.2 | CCERW precipitation and dynamical structure

198 The lagged composites of precipitation anomaly for the base point at 75°E in the Indian Ocean (Figure 3) show the  
199 westward propagation of the CCERW. At lag  $-3$  days (i.e., three days before the CCERWs cross the base point at  
200 75°E), there are positive precipitation anomalies in the sector from 70–100°E (Figure 3a). These are approximately  
201 symmetric about the equator, with off-equatorial maxima. This indeed appears to be similar to the spatial structure  
202 suggested by the lower-tropospheric convergence anomalies in the theoretical equatorial Rossby wave (Figure 1),  
203 described in Section 2.1. At lag 0 days, the precipitation anomalies have moved westward, to be centred at the base  
204 point at 75°E, by design (Figure 3b). The equatorial precipitation anomalies have weakened, so that the structure is  
205 now mainly composed of two off-equatorial maxima. At lag 3 days, the precipitation anomalies have moved further  
206 westward, to around 65°E (Figure 3c). The weak positive precipitation anomalies on the equator between these two  
207 off-equatorial maxima have now disappeared and been replaced by negative precipitation anomalies. Additionally, a  
208 developing larger scale region of negative precipitation anomalies from approximately 12°S–12°N has strengthened  
209 and also moved westward, behind (i.e., to the east of) the positive precipitation anomalies.

210 Note that these lagged composites of precipitation have been calculated from unfiltered precipitation anomalies.



211 The mean annual cycle was calculated and subtracted, but no wavenumber–frequency filtering was performed. The  
212 magnitudes of these unfiltered composite precipitation anomalies are up to  $5 \text{ mm day}^{-1}$ , which is approximately 50%  
213 of the value of the mean precipitation signal in this region. Hence, these CCERW precipitation anomalies constitute  
214 a very strong, robust signal.

215 The dynamical structure of the CCERWs is investigated through lagged composites of lower tropospheric (850  
216 hPa) dynamical variables (Figure 4), for comparison with the dynamical structure of theoretical equatorial Rossby  
217 waves (Figure 1) and as a prelude to the calculation of the CCERW vorticity budget. At lag  $-3$  days (Figure 4a), the  
218 convergence field (blue dotted line contours) matches well the regions of positive precipitation anomalies in Figure 3a,  
219 with an approximately equatorially symmetric band of convergence in the sector from  $70$ – $100^\circ\text{E}$ , with slightly weaker  
220 convergence on the equator and off-equatorial maxima in convergence off the equator around  $8^\circ$  latitude in both  
221 hemispheres. This latitudinal structure of the convergence anomalies in the CCERW bears a strong resemblance to  
222 the corresponding convergence anomalies in the theoretical equatorial Rossby wave (Figure 1).

223 The wind and vorticity anomalies in the CCERW also bear a strong similarity with the theoretical wave, with two  
224 off-equatorial cyclonic vorticity anomalies, with westerly anomalous flow on the equator in between them. However,  
225 we recall that in the theoretical equatorial Rossby wave (Figure 1), the convergence anomalies lay a quarter cycle to  
226 the east of the cyclone pair. In the CCERW (Figure 4a), the convergence anomalies are coincident (in phase) with  
227 the cyclone pair. Given the role of the convergence/divergence anomalies in retarding the westward propagation of  
228 the theoretical equatorial Rossby wave, this change in phase relationship will almost certainly have an impact on the  
229 propagation and possibly growth mechanisms in the CCERW.

230 By lag 0 days, the lower tropospheric cyclone pair and accompanying convergence (Figure 4b) and enhanced  
231 precipitation anomalies (Figure 3b) have moved westward to the base point at  $75^\circ\text{E}$ . By lag 3 days, the whole dynam-  
232 ical structure has moved further westward to  $65^\circ\text{E}$ . Within each of the lower tropospheric off-equatorial cyclonic  
233 anomalies, there is still convergence (Figure 4c) and enhanced precipitation (Figure 3c). However, on the equator the  
234 precipitation appears to have become decoupled from the dynamical structure, with reduced precipitation coincident  
235 with lower tropospheric convergence.

236 The change in structure in the vertical can be seen from the zero-lagged dynamical CCERW composites at se-  
237 lected levels: the boundary layer (975 hPa; Figure 5d); the free lower troposphere (850 hPa; Figure 5c); the middle  
238 troposphere (500 hPa; Figure 5b); the upper troposphere (200 hPa; Figure 5a). Overall, there is very little vertical tilt  
239 in the lower to middle troposphere, with the wind and vorticity structures stacking up at each level (Figure 5b–d). This  
240 is consistent with previous studies of CCERWs (Nakamura and Takayabu, 2022a; Inoue et al., 2020), and is in contrast  
241 to the structure of the gravity-type modes (CCKWs, convectively coupled mixed Rossby-gravity waves and eastward  
242 inertio-gravity waves) that show a pronounced upward tilt to the west, against their direction of propagation (Wheeler  
243 et al., 2000; Kiladis et al., 2009; Matthews, 2021).

244 Although the convergence regions in the CCERWs do remain co-located with the cyclonic vorticity anomalies  
245 throughout the lower to middle troposphere, their horizontal spatial structure does change with height. In the bound-  
246 ary layer at 975 hPa, the convergence is strong and almost entirely within the off-equatorial cyclonic vorticity anoma-  
247 lies (Figure 5d). In the free lower troposphere at 850 hPa, as previously noted, the the convergence is still strongest  
248 within the off-equatorial cyclonic vorticity anomalies, but there is also significant convergence along the equator (Fig-  
249 ure 5c). By the middle troposphere at 500 hPa, the strongest convergence is actually at the equator, with weaker  
250 convergence within the off-equatorial cyclonic vorticity anomalies (Figure 5b). At all levels in the lower to middle  
251 troposphere, the CCERW structure does resemble a modified theoretical equatorial Rossby wave.

252 However, the structure in the upper troposphere at 200 hPa is rather different (Figure 5a). The expected structure,  
253 assuming a first internal mode vertical structure, is of a similar spatial pattern to the lower troposphere, but with a

254 sign reversal. There is some evidence for this type of structure in the composite CCERW; at the longitude of the  
 255 base point (75°E) there is upper tropospheric divergence with off-equatorial maxima above the lower tropospheric  
 256 convergence. There is also a (weak) anticyclonic vorticity pair (negative in Northern Hemisphere, positive in Southern  
 257 Hemisphere) above the cyclonic vorticity pair in the lower troposphere. However, the vector wind field is different,  
 258 and is dominated by a large-scale divergent outflow both polewards (a local Hadley circulation) and eastwards (a local  
 259 Walker circulation). This is a major departure from the expected theoretical structure. Similar behaviour was also  
 260 observed in the upper tropospheric structure of CCKWs (Matthews, 2021). Hence, it appears that, apart from the  
 261 horizontal phase relationship between vorticity and divergence, convectively coupled equatorial waves in general bear  
 262 some resemblance to their theoretical counterparts in the lower troposphere, but have a radically different, divergent  
 263 outflow structure in the upper troposphere.

### 264 3.3 | CCERW vorticity budget

265 Given that the 850 hPa free lower tropospheric structure of the CCERW is fairly representative of the structure  
 266 throughout the lower and middle troposphere, a vorticity budget of the CCERW is carried out at this level, to ascer-  
 267 tain the dynamical propagation and growth mechanisms. The seven individual vorticity source terms are shown in  
 268 Figure 6a–g. These have been spatially smoothed using triangular truncation in spectral space at total wavenumber  
 269 42 (Dawson, 2016).

270 The planetary vorticity advection ( $-\beta v$ ) term (Figure 6f) in the CCERW has positive tendencies (colour shading)  
 271 to the west of positive vorticity anomalies (line contours) and negative tendencies to the east. Hence, this Rossby  
 272 wave propagation mechanism still contributes strongly to westward propagation of the CCERW, just as it does in the  
 273 theoretical equatorial Rossby wave (Figure 2a). It would be difficult to conceive of a situation where this was not the  
 274 case, as a cyclonic anomaly has, almost by definition, equatorward flow to the west, which will then advect high value  
 275 (cyclonic) potential vorticity to the west, leading to westward propagation.

276 The only other non-zero vorticity source term in the theoretical equatorial Rossby wave was the vortex stretching  
 277 ( $-fD$ ) term (Figure 2b). As discussed in Section 2.2, the quarter cycle phase difference between the vorticity and  
 278 divergence fields led to a (weak) eastward propagation tendency. However, in the CCERW, the convergence anomaly  
 279 is in phase with the cyclonic vorticity, leading to growth rather than propagation (positive tendency in phase with the  
 280 positive vorticity in Figure 6e).

281 If the CCERW behaved like the theoretical equatorial Rossby wave, then the remaining five vorticity source terms  
 282 (Figure 6a–d, g) would be zero. This is clearly not the case. The other vortex stretching term ( $-\zeta D$ ; Figure 6d), from  
 283 the non-linear interaction between relative vorticity and divergence, also has positive vorticity tendencies in phase  
 284 with positive vorticity anomalies. Hence, this term also leads to growth.

285 There are also strong contributions from the two horizontal advection terms. The zonal advection ( $-u\partial\zeta/\partial x$ ;  
 286 Figure 6a) term has quite a complex spatial structure. It is strongest in the Northern Hemisphere, with a large negative  
 287 tendency at the location of the positive vorticity anomaly at 75°E, 10°N, and a large positive tendency at the location  
 288 of the negative vorticity anomaly at 100°E, 10°N. These vorticity tendencies will destructively interfere with the  
 289 vorticity pattern, leading to decay of the CCERW. The situation in the Southern Hemisphere is opposite, with, for  
 290 example, a negative tendency at the location of the negative vorticity anomaly at 75°E, 10°S, leading to growth.  
 291 However, the anomalies in the Southern Hemisphere are considerably weaker, and the overall behaviour will likely be  
 292 dominated by the Northern Hemisphere structure.

293 The meridional advection ( $-v\partial\zeta/\partial y$ ; Figure 6b) term also has a complex spatial structure. This is strongest in  
 294 the Southern Hemisphere where the tendency and vorticity anomalies are out of phase, leading to decay. However,

295 in the Northern Hemisphere, the positive tendency at 85°E, 10°N is to the east of the positive vorticity anomaly at  
 296 75°E, 10°N, leading to an eastward propagation tendency. The total horizontal advection term (Figure 6h; the sum  
 297 of panels a and b) shows more clearly the net effect of horizontal advection, which is to destructively interfere with  
 298 the vorticity pattern, leading to decay. The vertical advection (Figure 6c) and the tilting/twisting term (Figure 6g) are  
 299 both weak and will contribute little to propagation or growth.

300 The propagation and growth characteristics of each vorticity source term are quantified in a polar propagation–  
 301 growth diagram (Figure 7). The methodology is described in full detail in Matthews (2021). To summarise, a domain  
 302 of interest is first defined, centred on the base point at 75°E and the equator (55–95°E, 18°S–18°N). For a particular  
 303 vorticity source term of interest, the root mean square (RMS) amplitude of that vorticity source term over the domain  
 304 is calculated, and then normalised by the RMS amplitude of the vorticity tendency ( $\partial\zeta/\partial t$ ) term. Then, cosine waves  
 305 in the zonal direction are fitted to the vorticity anomaly, and the vorticity source term over the domain. The phase  
 306 difference between the vorticity field and the vorticity source term is then the phase difference between these two  
 307 cosine waves; this is expressed as a multiple of  $\tau$  (radians), where  $\tau = 2\pi \approx 6.283 \dots$  radians is equivalent to one full  
 308 turn (Abbott, 2012)<sup>1</sup>. These two quantities (normalised RMS amplitude, phase difference) are plotted as a point on  
 309 the polar propagation–growth diagram (Figure 7).

310 By construction, the point for the vorticity tendency  $\partial\zeta/\partial t$  term lies very close to the position (1.00,  $-0.25\tau$ ) as its  
 311 normalised amplitude (normalised by itself) is 1, and the vorticity tendency (of a propagating wave) is a quarter cycle  
 312 out of phase with the vorticity. The diagram is oriented so that a phase difference of  $-0.25\tau$  (leading by a quarter  
 313 cycle) is on the left side of the diagram, indicating westward propagation; a phase difference of  $0.25\tau$  (lagging by a  
 314 quarter cycle) is on the right side, indicating eastward propagation; a phase difference of 0 (in phase) is at the top,  
 315 indicating growth; and a phase difference of  $0.5\tau$  (out of phase) is on the bottom, indicating decay.

316 The planetary vorticity advection  $-\beta v$  term has large amplitude, and is in the blue westward-propagating quad-  
 317 rant, indicating it is the term that contributes most strongly to the westward propagation of the CCERW. Both vortex  
 318 stretching terms ( $-fD$  and  $-\zeta D$ ) are in the red growth quadrant, and vortex stretching is evidently the process by  
 319 which the CCERW grows. The horizontal advection terms both lie in the red decay quadrant, with the meridional  
 320 advection term also contributing to a slight eastward propagation tendency. The total horizontal advection term (sum  
 321 of zonal and meridional advection) lies between these two, as expected, in the decay quadrant. The remaining terms  
 322 (vertical advection and tilting/twisting) lie near the centre of the diagram as their amplitudes are weak. They do not  
 323 contribute significantly to the vorticity budget.

324 The total source term  $S$ , shown by the purple marker, lies in the westward propagating quadrant, but also on the  
 325 edge of the growth quadrant, thus the net effect of all the source terms is one of westward propagation and growth.  
 326 The residual term  $\epsilon$  (yellow marker in Figure 7) is calculated as the difference between the vorticity tendency  $\partial\zeta/\partial t$   
 327 and total source  $S$  terms. It represents sub-grid scale terms that are not explicitly calculated by the other vorticity  
 328 source terms, plus any numerical errors in the calculation of the individual source terms due to discretisation (gridding)  
 329 of the data. As sub-grid scale terms tend to be generally diffusive, it is not surprising that this term lies in the decay  
 330 quadrant. The magnitude of the residual term (distance from the centre of the polar plot) is larger than those of  
 331 the vertical advection and tilting terms, similar to those of the vortex stretching and horizontal advection terms, and  
 332 smaller than the dominant advection of planetary vorticity term. Hence, sub-grid scale processes / numerical errors  
 333 certainly contribute to the overall vorticity budget.

334 Finally, for comparison, the vorticity budget terms from the theoretical equatorial Rossby wave are shown by  
 335 square markers in Figure 7. These lie on the pure propagation line in the diagram, with the planetary vorticity advection  
 336  $-\beta v$  term contributing strongly to westward propagation, and the vortex stretching  $-fD$  term contributing weakly

<sup>1</sup>Hence, for example, a quarter cycle is written as the more natural  $\tau/4$  radians, rather than the unintuitive  $\pi/2$  radians.

337 to eastward propagation. The total source  $S$  terms lies at the point  $(1.00, -0.25\tau)$ , corresponding to pure westward  
338 propagation with no growth.

## 339 4 | CONCLUSIONS

340 The dynamical mechanisms of propagation and growth in observed CCERWs were analysed via a vorticity budget of  
341 ERA5 reanalysis data using a database of CCERW events calculated from IMERG precipitation. This was compared  
342 with a vorticity budget of theoretical equatorial Rossby waves, under the hypothesis that CCERWs would act dynam-  
343 ically like modified versions of those theoretical waves.

344 As anticipated, the main mechanism for westward propagation of CCERWs is through advection of planetary  
345 vorticity (the  $-\beta v$  term), i.e., the standard Rossby wave propagation mechanism. Equatorward flow to the west of  
346 the off-equatorial cyclonic anomalies advects high magnitude (cyclonic) planetary vorticity into the region west of  
347 the original cyclonic anomaly. Poleward flow to the east of the off-equatorial cyclonic anomalies advects low mag-  
348 nitude (anticyclonic) planetary vorticity into the region east of the original cyclonic anomaly, and west of the trailing  
349 anticyclonic anomaly. The net result is a westward propagation of the vorticity pattern.

350 In the theoretical equatorial Rossby wave, linear vortex stretching (the  $-fD$  term) gives a weak eastward propaga-  
351 tion tendency. The convergence in the theoretical wave lies to the east of the off-equatorial cyclonic anomalies, from  
352 negative  $\partial u/\partial x$  on the equator and negative  $\partial v/\partial y$  off the equator. This leads to vortex stretching and a cyclonic  
353 vorticity tendency to the east of the cyclonic vorticity anomalies, and hence an eastward propagation tendency. This  
354 acts to effectively slow the westward phase speed of the theoretical wave from its non-divergent equivalent.

355 However, this mechanism is very different in the CCERWs. In the lower troposphere, convergence is in phase with  
356 the off-equatorial cyclonic anomalies. The resulting cyclonic vorticity tendency from vortex stretching at the same  
357 location as the cyclonic vorticity anomalies leads to growth of the CCERW. Both the linear ( $-fD$ ) and non-linear ( $-\zeta D$ )  
358 vortex stretching terms contribute to this growth. This change in the role of vortex stretching, from a weak eastward  
359 propagation tendency in the theoretical wave to growth in the CCERW, will lead to an effective increase in the actual  
360 westward propagation speed of the CCERW, by up to 25%. The horizontal vorticity advection and the sub-gridscale  
361 terms also have important roles and act to dampen the CCERW. The total vorticity source for CCERWs is one of both  
362 westward propagation and slight growth. This contrasts with the total vorticity source for the theoretical equatorial  
363 Rossby waves, which is one of pure westward propagation.

364 In the upper troposphere, the CCERW structure is quite different, and is dominated by a large-scale divergent  
365 outflow, rather than an equatorial Rossby-wave like structure. This is perhaps not surprising when the background  
366 flow in the region is considered. Over the Indian Ocean, the background flow in the lower troposphere is typically  
367 a weak westerly, while in the upper troposphere it is a strong easterly, with a resulting vertical shear of up to 20  
368  $\text{m s}^{-1}$  over the depth of the troposphere. This will act to shear out any vertical modal structure present, and one of  
369 the major, limiting assumptions in the traditional, theoretical, linear equatorial wave analysis is that the background  
370 flow is zero (and therefore has zero vertical shear). In reality, it appears that the CCERW structure is set by equatorial  
371 Rossby wave dynamics interacting with convection in the lower troposphere, with a divergent outflow structure aloft.

372 These results have implications for modelling of CCERWs, and prediction of CCERW-related precipitation and  
373 wind fields in climate modelling and numerical weather forecasting frameworks. Models need to correctly simulate  
374 the internal structure of CCERWs, especially the phase relationships between vorticity and divergence, to correctly  
375 simulate growth rates and propagation speeds. Errors in growth rates will lead to incorrect predictions of the strength  
376 of a CCERW system, and errors in propagation speed will lead to incorrect predictions in the timing of arrival of

377 CCERW-related weather phenomena (e.g., extreme precipitation, winds). The CCERW event and vorticity budget  
378 diagnostics presented here can also be applied to numerical weather prediction (NWP) data to assess model fidelity  
379 in simulating these CCERW processes.

380 CCERWs and other equatorial wave structures can now be readily identified in real-time data, and this infor-  
381 mation used to inform real-time forecasts (Yang et al., 2021). Indeed, the importance of correctly simulating the  
382 dynamical structures of CCERWs has been highlighted recently (Ferrett et al., 2023), even if the model concerned  
383 has less skill in predicting the precipitation structures associated with CCERWs. Here, the ability of a forecast model  
384 to skillfully predict the dynamical development of CCERWs was combined with the known observed relationship be-  
385 tween extreme precipitation and the CCERW dynamical structure, to produce hybrid dynamical–statistical forecasts  
386 of CCERW-related extreme precipitation. The skill of this hybrid model exceeds the skill of the actual NWP simulated  
387 precipitation (i.e., the direct precipitation forecast) over the South Philippines and in central Vietnam. This system is  
388 still in its relative infancy, but has high potential for the future of predicting CCERW-associated extreme precipitation

389 This study investigated the dynamical mechanisms behind propagation and growth in a CCERW, using a vorticity  
390 budget. It is therefore only a partial analysis of the driving mechanisms behind CCERWs. Of course the mechanism  
391 behind the coupling of convection and the dynamics is also crucial and, one could argue, more fundamental.

392 CCERW convection is observed to be in phase with the total column water anomaly, and convection in the active  
393 region of CCERWs is actually due to mesoscale convective systems being triggered there (Nakamura and Takayabu,  
394 2022b). The existence of the total column water anomaly is likely to be due to (moisture) convergence. The moist  
395 convection then leads to large-scale ascent and spin up of vorticity through the vortex stretching ( $-fD$  and  $-\zeta D$   
396 terms). Hence, cyclonic vorticity in the CCERW is in phase with lower tropospheric convergence. As seen from the  
397 vorticity budget analysis presented here, this in-phase relationship is crucial for the growth of the CCERWs, and also  
398 the CCERW propagation speed, as it removes the eastward retarding tendency of the  $-fD$  term that exists in the dry  
399 theoretical waves, effectively speeding up the coupled wave from its theoretical counterpart.

400 Theoretical and numerical analyses using the moisture mode and WISHE frameworks have also established the  
401 link between theoretical equatorial Rossby waves and CCERW-type structures. Fuchs-Stone et al. (2019) found that  
402 the the equatorial Rossby wave in a dry atmosphere transitioned to a westward-propagating WISHE–moisture mode  
403 (CCERW analogue) when convection was switched on. The westward propagation speed of the wave decreased  
404 when the convective coupling was allowed, mainly due to WISHE and cloud–radiation interactions. A thermodynamic  
405 instability was found, from interactions between surface fluxes and atmospheric moisture. Further analysis within the  
406 WISHE framework found that a background easterly flow and pre-moistening by WISHE contributed to the westward  
407 propagation of the mode, and that growth occurred through destabilisation by WISHE and the background easterly  
408 shear (Chen, 2022).

409 Several lines for future work present themselves. The dynamical analysis presented here through the vorticity  
410 budgets, and the previous thermodynamical analyses using the WISHE and moisture mode frameworks should be self-  
411 consistent and a combined analysis of CCERWs using both these approaches is desirable. Also, there is an interesting  
412 question of how and why does the transition in structure (in particular the phasing between vorticity and divergence)  
413 between an idealised dry equatorial Rossby wave to a fully fledged moist CCERW come about, as processes such as  
414 boundary layer friction and the strength of the convective coupling is increased.

415 The focus in this study was on the Indian Ocean, as the large ocean basin with fairly homogeneous SST distribu-  
416 tions was considered likely to lead to the simplest and most generally applicable analysis of the CCERW dynamical  
417 structures. It is an open question whether the same relationships will hold in the other regions of the tropics. How will  
418 the complex island geometry of the Maritime Continent affect the CCERW structures? Will the warm SSTs and narrow  
419 ITCZs north of equator in the Pacific and Atlantic basins have a major effect? How will land–atmosphere interactions

over Africa and South America affect the CCERW phase relationships documented here?

This vorticity budget approach has been applied to CCKWs (Matthews, 2021), and in this study to CCERWs. Other convectively coupled equatorial waves, such as mixed Rossby–gravity waves should also be amenable to this type of analysis. Indeed, vorticity diagnostics of convectively coupled mixed Rossby–gravity waves have already been shown to be useful in analysing their role in the generation of African easterly waves (Yang et al., 2018).

In summary, a vorticity budget framework has been presented for CCERWs to explain their propagation and growth characteristics, from a dynamical-only perspective, over the Indian Ocean. This approach appears to have potential in diagnosing climate and NWP model errors, and in a wider thermodynamical–dynamical analysis of convectively coupled equatorial waves.

## ACKNOWLEDGEMENTS

The research presented in this paper was carried out on the High Performance Computing Cluster supported by the Research Computing Service at the University of East Anglia. AJM was partially supported by the Natural Environment Research Council through the TerraMaris project (grant NE/R016704/1). I thank the three anonymous reviewers whose comments helped to improve the manuscript.

## DATA AVAILABILITY

All data used in this analysis are publicly available. The IMERG precipitation data were supplied by the National Aeronautics and Space Administration through their web site at [gpm.nasa.gov](https://gpm.nasa.gov). ERA-5 data were accessed from Copernicus at <https://cds.climate.copernicus.eu> (doi: 10.24381/cds/bd0915c6). The python code used for the analysis is archived at <https://github.com/adrianjmatthews/py36/>.

## references

- Abbott, S. (2012) My conversion to tauism. *Math Horizons*, **19**, 34.
- Baranowski, D. B., Flatau, M. K., Flatau, P. J., Karnawati, D., Barabasz, K., Labuz, M., Latos, B., Schmidt, J. M., Paskf, J. A. I. and Marzuki (2020) Social-media and newspaper reports reveal large-scale meteorological drivers of floods on Sumatra. *Nature Communicat.*, **11**, 2503.
- Baranowski, D. B., Flatau, M. K., Flatau, P. J. and Matthews, A. J. (2016) Impact of atmospheric convectively-coupled Kelvin waves on upper ocean variability. *J. Geophys. Res.*, **121**, 2045–2059.
- Chen, G. (2022) A model of the convectively coupled equatorial Rossby wave over the Indo-Pacific warm pool. *Atmos. Sci.*, **79**, 2267–2283.
- Dawson, A. (2016) Windspharm: A high-level library for global wind field computations using spherical harmonics. *J. Open. Res. Soft.*, **4**, e31.
- Dias, J., Gehne, M., Kiladis, G. N. and Magnusson, L. (2023) The role of convectively coupled equatorial waves in sub-seasonal predictions. *Geophys. Res. Lett.*, **21**, e2023GL106198.
- Diong, J. Y., Xavier, P., Woolnough, S. J. and Abdullah, F. A. (2023) Equatorial Rossby waves on cold surge days and their impact on rainfall. *Quart. J. Roy. Meteorol. Soc.*, **149**, 2031–2047.
- Feng, X., Yang, G. Y., Hodges, K. I. and Methven, J. (2023) Equatorial waves as useful precursors to tropical cyclone occurrence and intensification. *Nature Comm.*, **14**, 511.
- Ferrett, S., Methven, J., Woolnough, S. J., Yang, G. Y., Holloway, C. E. and Wolf, G. (2023) Hybrid dynamical-statistical forecasts of the risk of rainfall in South East Asia dependent on equatorial waves. *Mon. Weath. Rev.*, **151**, 2139–2152.
- Ferrett, S., Yang, G. Y., Woolnough, S., Methven, J., Hodges, K. and Holloway, C. E. (2020) Linking extreme precipitation in southeast Asia to equatorial waves. *Quart. J. Roy. Meteorol. Soc.*, **146**, 665–684.
- Frank, W. M. and Roundy, P. E. (2006) The role of tropical

- 478 waves in tropical cyclogenesis. *Mon. Weath. Rev.*, **124**,  
479 2397–2417. 524
- 480 Fuchs-Stone, Z., Raymond, D. J. and Sentic, S. (2019) A simple  
481 model of convectively coupled equatorial Rossby waves.  
482 *J. Adv. Model. Earth Sys.*, **11**, 173–184. 527
- 483 Gill, A. E. (1982) *Atmosphere-ocean dynamics*. Academic  
484 Press. 530
- 485 Hersbach, H., Bell, B., Berrisford, P., Hirahara, S., Horanyi, A.,  
486 Munoz-Sabater, J., Nicolas, J., Peubey, C., Radu, R., Schep-  
487 pers, D., Simmons, A., Soci, C., Abdalla, S., Abellan, X., Bal-  
488 samo, G., Bechtold, P., Biavati, G., Bidlot, J., Bonavita, M.,  
489 De Chiara, G., Dahlegren, P., Dee, D., Diamantakis, M.,  
490 Dragani, R., Flemming, J., Forbes, R., Fuentes, M., Geer, A.,  
491 Haimberger, L., Healy, S., Hogin, R. J., Holm, E., Janisková,  
492 M., Keeley, S., Laloyaux, P., Lopez, P., Lupu, C., Radnoti,  
493 G., de Rosnay, P., Rozum, I., Vamborg, F., Villaume, S. and  
494 Thepaut, J. N. (2020) The ERA5 global reanalysis. *Quart. J. Roy. Meteorol. Soc.*, **146**, 1999–2049. 539
- 495 540
- 496 Huffman, G. J., Stocker, E. F., Bolvin, D. T., Nelkin, E. J. and Tan  
497 J. (2019) GPM IMERG final precipitation L3 half hourly 0.1  
498 degree x 0.1 degree V06. 542
- 499 Inoue, K., Adames, A. F. and Yasunaga, K. (2020) Vertical  
500 velocity profiles in convectively coupled equatorial waves  
501 and the MJO: New diagnoses of vertical velocity profiles  
502 in the wavenumber-frequency domain. *J. Atmos. Sci.*, **77**,  
503 2139–2162. 547
- 504 Janicot, S., Mounier, F., Gervois, S., Sultan, B. and Kiladis, G. N.  
505 (2010) The dynamics of the West African monsoon. Part  
506 V: The detection and role of the dominant modes of con-  
507 vectively coupled equatorial Rossby waves. *J. Climate*, **23**,  
508 4005–4024. 552
- 509 Kemball-Cook, S. and Wang, B. (2001) Equatorial waves and  
510 air-sea interaction in the Boreal Summer Intraseasonal Os-  
511 cillation. *J. Climate*, **14**, 2923–2942. 555
- 512 Kiladis, G. N., Wheeler, M. C., Haertel, P. T., Straub, K. S.,  
513 and Roundy, P. E. (2009) Convectively coupled equatorial  
514 waves. *Rev. Geophys.*, **47**, RG2003. 558
- 515 Knippertz, P., Gehne, M., Kiladis, G. N., Kikuchi, K., Satheesh,  
516 A. R., Roundy, P. E., Yang, G. Y., Zagar, N., Dias, S. D.,  
517 Fink, A. H., Methven, J., Schlueter, A., Sielmann, F. and  
518 Wheeler, M. C. (2022) The intricacies of identifying equa-  
519 torial waves. *Quart. J. Roy. Meteorol. Soc.*, **148**, 2814–  
520 2852. 563
- 521 Latos, B., Lefort, T., Flatau, M. K., Flatau, P. J., Permana, D. S.,  
522 Baranowski, C. B., Paski, J. A. I., Makmur, E., Sulystyo, S.,  
Peyrille, P., Feng, Z., Matthews, A. J. and Schmidt, J. M.  
(2021) Equatorial waves triggering extreme rainfall and  
floods in southwest Sulawesi, Indonesia. *Mon. Weath. Rev.*,  
**149**, 1381–1401.
- Latos, B., Peyrille, P., Lefort, T., Baranowski, D. B., Flatau,  
M. K., Flatau, P. J., Florida Riama, N., Permana, D. S., Ryd-  
beck, A. V. and Matthews, A. J. (2023) The role of tropical  
waves in the genesis of Tropical Cyclone Seroja in the Mar-  
itime Continent. *Nature Comm.*, **14**, 856.
- Matsuno, T. (1966) Quasi-geostrophic motions in the equato-  
rial area. *J. Meteorol. Soc. Japan*, **44**, 25–42.
- Matthews, A. J. (2021) Dynamical propagation and growth  
mechanisms for convectively coupled equatorial Kelvin  
waves over the Indian Ocean. *Quart. J. Roy. Meteorol. Soc.*,  
**147**, 4310–4336.
- Meehl, G. A., Lukas, R., Kiladis, G. N., Weickmann, K. M.,  
Matthews, A. J. and Wheeler, M. (2001) A conceptual  
framework for time and space scale interactions in the cli-  
mate system. *Climate Dyn.*, **17**, 753–775.
- Nakamura, Y. and Takayabu, Y. N. (2022a) Convective cou-  
plings with equatorial Rossby waves and equatorial Kelvin  
waves. Part I: Coupled wave structures. *J. Atmos. Sci.*, **79**,  
247–262.
- (2022b) Convective couplings with equatorial Rossby  
waves and equatorial Kelvin waves. Part II: Coupled pre-  
cipitation characteristics. *J. Atmos. Sci.*, **79**, 247–262.
- Takayabu, Y. N. (1994) Large-scale cloud disturbances associ-  
ated with equatorial waves. Part I: Spectral features of the  
cloud disturbances. *J. Meteorol. Soc. Japan*, **72**, 433–448.
- Tsai, W. Y. H., Lu, M. M., Sui, C. H. and Lin, P. H. (2020) MJO  
and CCEW modulation on South China Sea and Maritime  
Continent boreal winter subseasonal peak precipitation.  
*Terrest. Atmos. Ocean. Sci.*, **31**, 177–195.
- Wheeler, M. and Kiladis, G. N. (1999) Convectively coupled  
equatorial waves: Analysis of clouds and temperature in  
the wavenumber-frequency domain. *J. Atmos. Sci.*, **56**,  
374–399.
- Wheeler, M., Kiladis, G. N. and Webster, P. J. (2000) Large-  
scale dynamical fields associated with convectively cou-  
pled equatorial waves. *J. Atmos. Sci.*, **57**, 613–640.
- Yang, G. Y., Ferrett, S., Woolnough, S., Methven, J. and Hol-  
loway, C. (2021) Real-time identification of equatorial  
waves and evaluation of waves in global forecasts. *Weath.  
Forecast.*, **36**, 171–193.

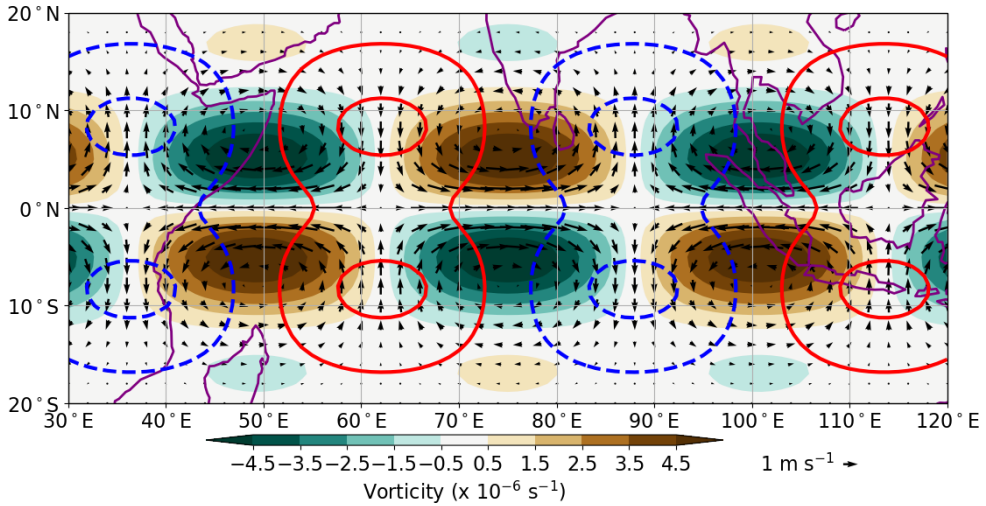


**FIGURE 1** Structure of a sample theoretical linear equatorial Rossby wave with zonal wavenumber 7 ( $k = 1.10 \times 10^{-6} \text{ m}^{-1}$ ), gravity wave phase speed  $c_g = 12 \text{ m s}^{-1}$ , and amplitude  $v_0 = 1 \text{ m s}^{-1}$ . Horizontal wind vectors are shown by the black arrows (scale vector has length  $1 \text{ m s}^{-1}$ ). Relative vorticity is colour shaded, with interval  $1 \times 10^{-6} \text{ s}^{-1}$ ; first positive contour is at  $0.5 \times 10^{-6} \text{ s}^{-1}$ . Divergence is shown by the thick line contours with interval  $0.3 \times 10^{-6} \text{ s}^{-1}$ ; positive contours are solid red and the first positive contour is at  $0.15 \times 10^{-6} \text{ s}^{-1}$ , negative contours are blue dashed. Continental outlines are shown in purple for scale only.

- 567 Yang, G. Y., Hoskins, B. J. and Slingo, J. M. (2003) Convectively  
 568 coupled equatorial waves: A new methodology for identifying  
 569 wave structures in observational data. *J. Atmos. Sci.*, **60**, 1637–1654.
- 570
- 571 Yang, G. Y., Methven, J., Woolnough, S., Hodges, K. and  
 572 Hoskins, B. (2018) Linking African easterly wave activity  
 with equatorial waves and the influence of Rossby waves  
 from the Southern Hemisphere. *J. Atmos. Sci.*, **75**, 1783–  
 1809.
- 576 Zhao, H. and Wu, L. (2018) Modulation of convectively cou-  
 pled equatorial Rossby wave on the western North Pacific  
 tropical cyclones activity. *Int. J. Climatol.*, **38**, 932–948.



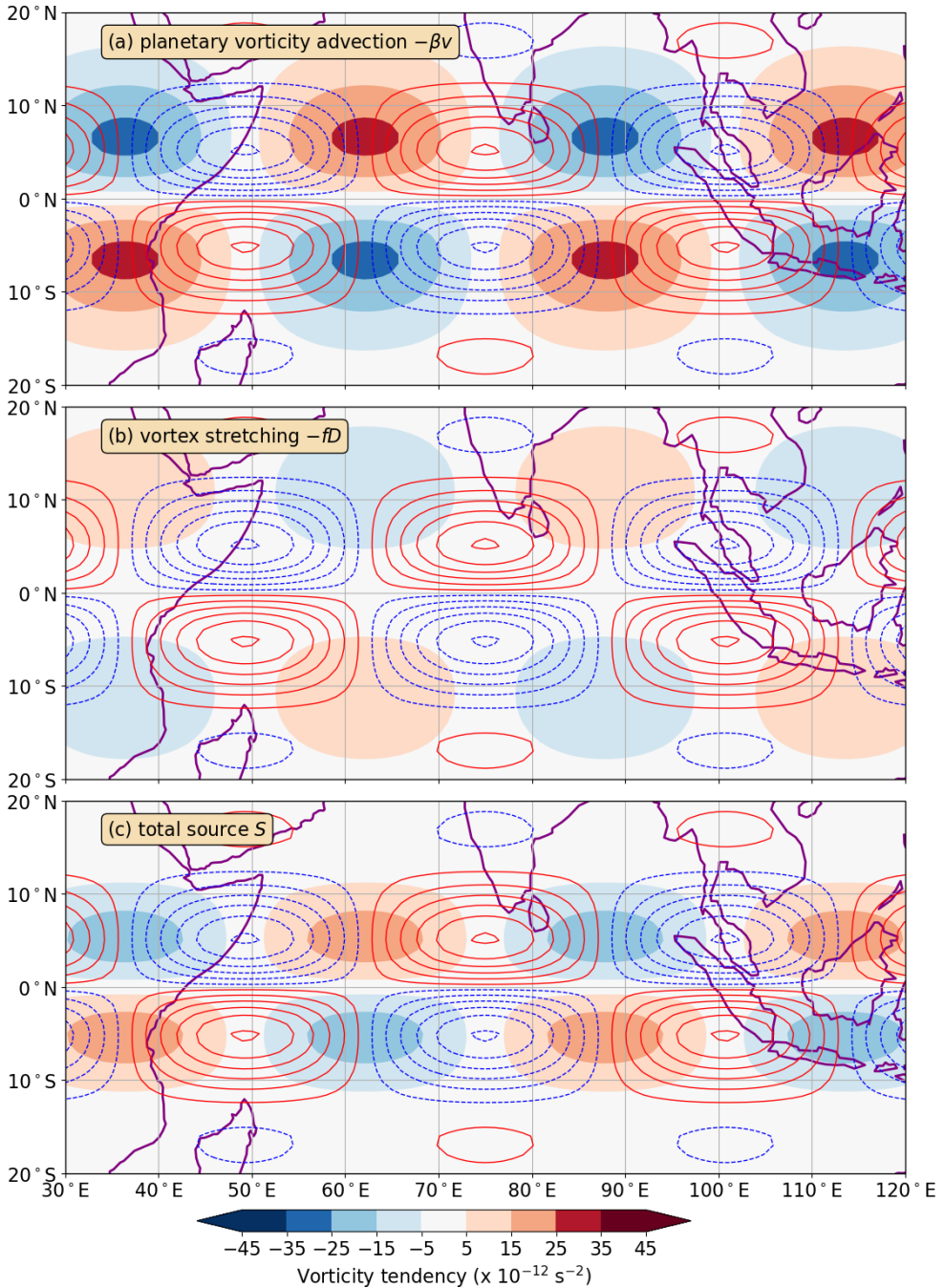


**FIGURE 2** Vorticity source terms of the theoretical linear equatorial Rossby wave in Figure 1: (a) planetary vorticity advection  $-\beta v$ , (b) vortex stretching  $-fD$ , (c) total vorticity source (equal to vorticity tendency). Colour shading interval is  $10 \times 10^{-12} \text{ s}^{-2}$ ; first positive level is at  $5 \times 10^{-12} \text{ s}^{-2}$ . The vorticity anomaly is shown by line contours; interval is  $1 \times 10^{-6} \text{ s}^{-1}$ , positive contours are solid red and first positive contour is at  $0.5 \times 10^{-6} \text{ s}^{-1}$ , and negative contours are dashed blue.

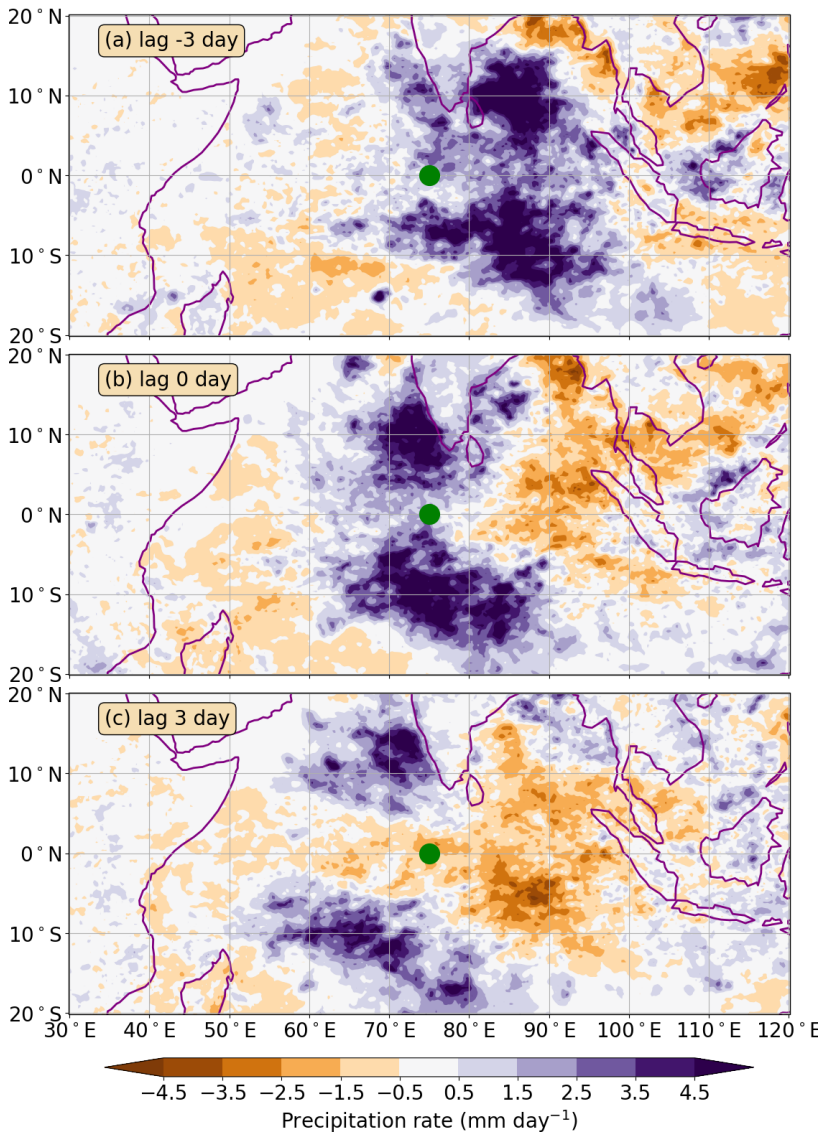


**FIGURE 3** Lagged composite maps of precipitation anomalies for CCERW over the Indian Ocean at lag (a) -3, (b) 0, (c) 3 days. Precipitation contour interval is 1 mm day<sup>-1</sup>. The base point at 75°E is shown by the green filled circle.

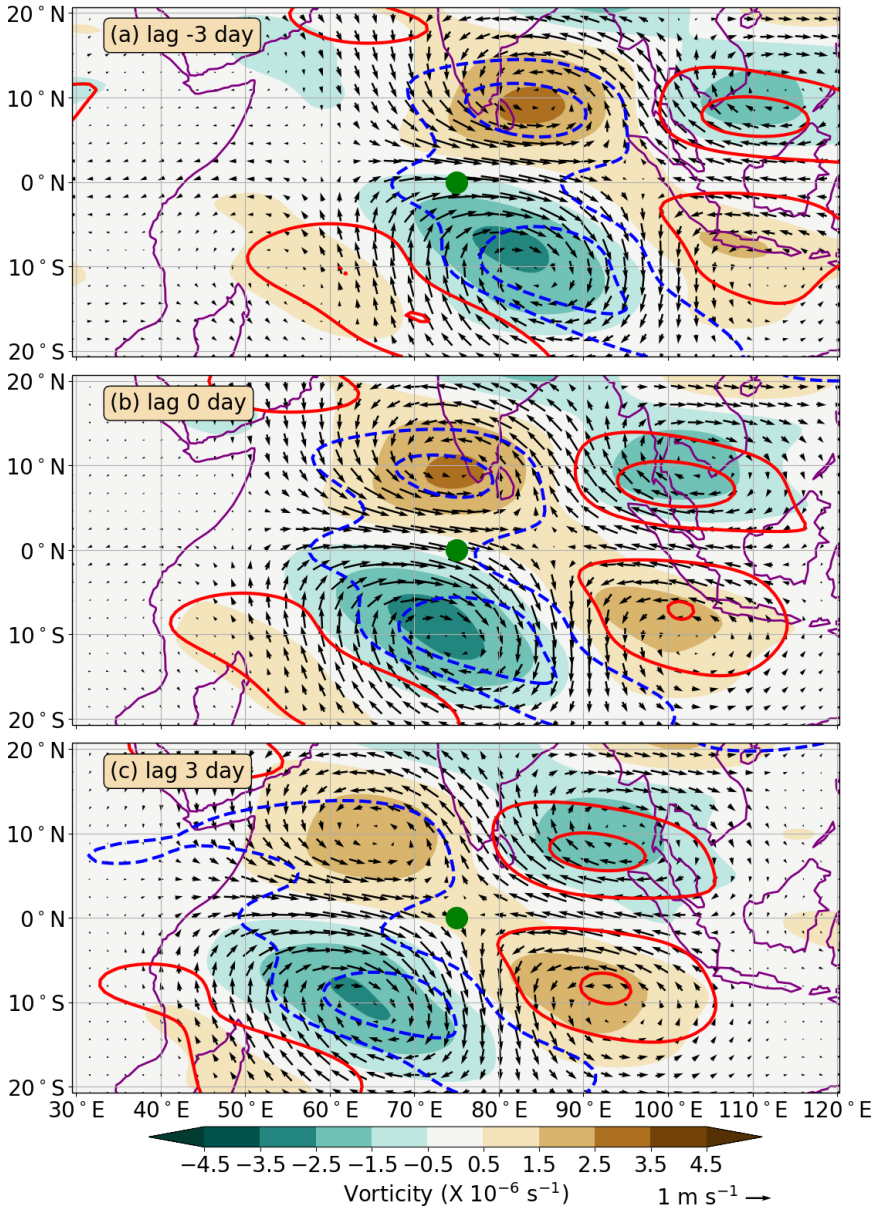


**FIGURE 4** Lagged composite maps of dynamical anomalies of CCERW at 850 hPa, for day (a) -3, (b) 0, (c) +3. Horizontal wind vectors are shown by the black arrows (scale vector has length 1 m s<sup>-1</sup>). Relative vorticity is colour shaded, with interval 1 × 10<sup>-6</sup> s<sup>-1</sup>; the first positive contour is at 0.5 × 10<sup>-6</sup> s<sup>-1</sup>. Divergence is shown by line contours with interval 0.25 × 10<sup>-6</sup> s<sup>-1</sup>; positive contours are solid red with the first positive contour at 0.125 × 10<sup>-6</sup> s<sup>-1</sup>, and negative contours are dashed blue. The dynamical fields were wavenumber–frequency filtered for CCERW signals before compositing.

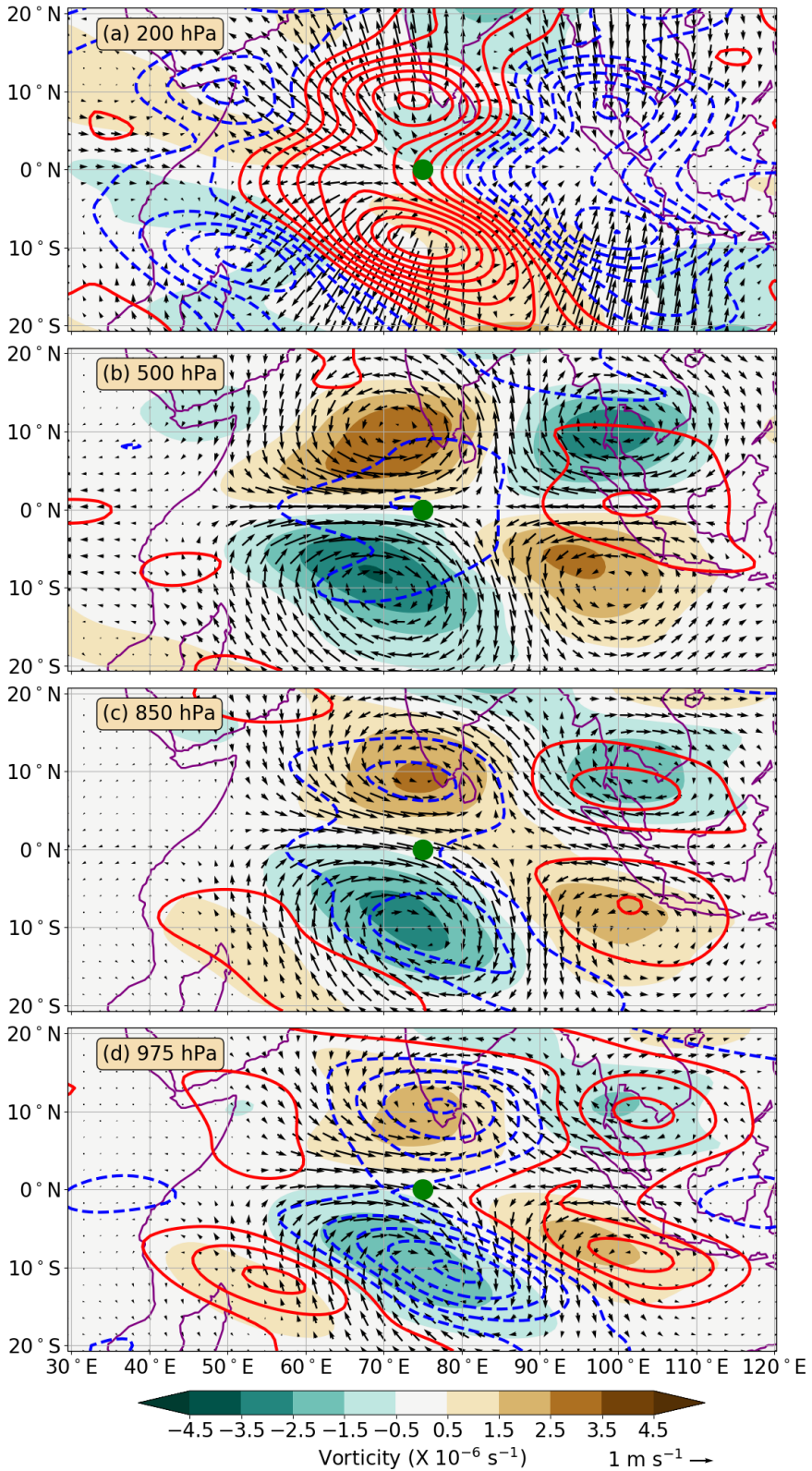


**FIGURE 5** Zero-lagged composite maps of dynamical anomalies of CCERW at (a) 200 hPa, (b) 500 hPa, (c) 850 hPa, (d) 975 hPa. Conventions as in Figure 4.

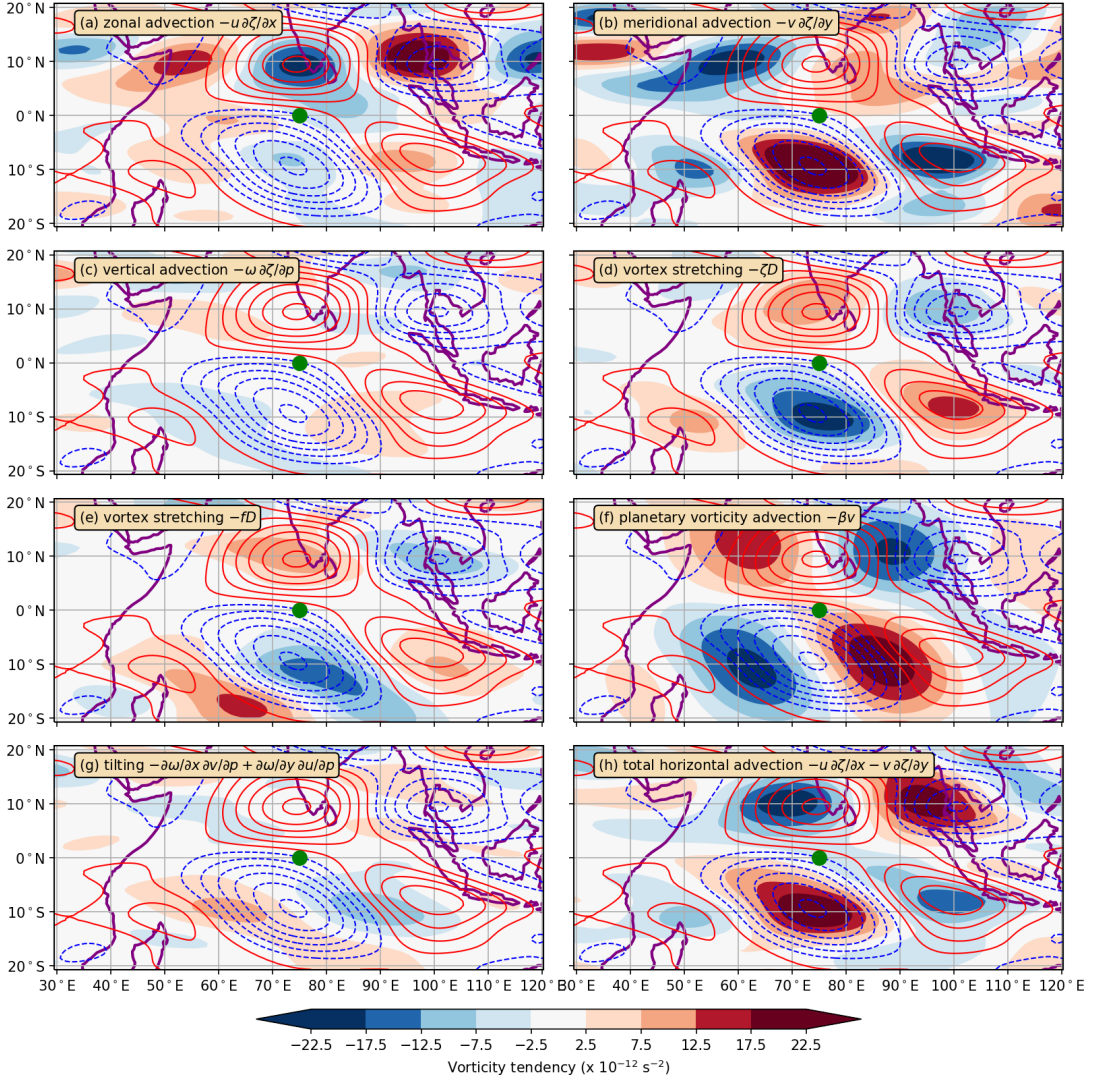


**FIGURE 6** Zero-lagged composite maps of individual source terms in vorticity budget of CCERW at 850 hPa: (a) zonal advection  $-u\partial\zeta/\partial x$ , (b) meridional advection  $-v\partial\zeta/\partial y$ , (c) vertical advection  $-\omega\partial\zeta/\partial p$ , (d) vortex stretching  $-\zeta D$ , (e) vortex stretching  $-fD$ , (f) planetary vorticity advection  $-\beta v$ , (g) tilting  $-\partial\omega/\partial x \partial v/\partial p + \partial\omega/\partial y \partial u/\partial p$ , (h) total horizontal advection  $-u\partial\zeta/\partial x - v\partial\zeta/\partial y$ . Colour shading interval is  $5 \times 10^{-12} \text{ s}^{-2}$ ; first positive level is at  $2.5 \times 10^{-12} \text{ s}^{-2}$ . The vorticity anomaly is shown by line contours; interval is  $0.5 \times 10^{-6} \text{ s}^{-1}$ , positive contours are solid red and first positive contour is at  $0.25 \times 10^{-6} \text{ s}^{-1}$ , and negative contours are dashed blue.

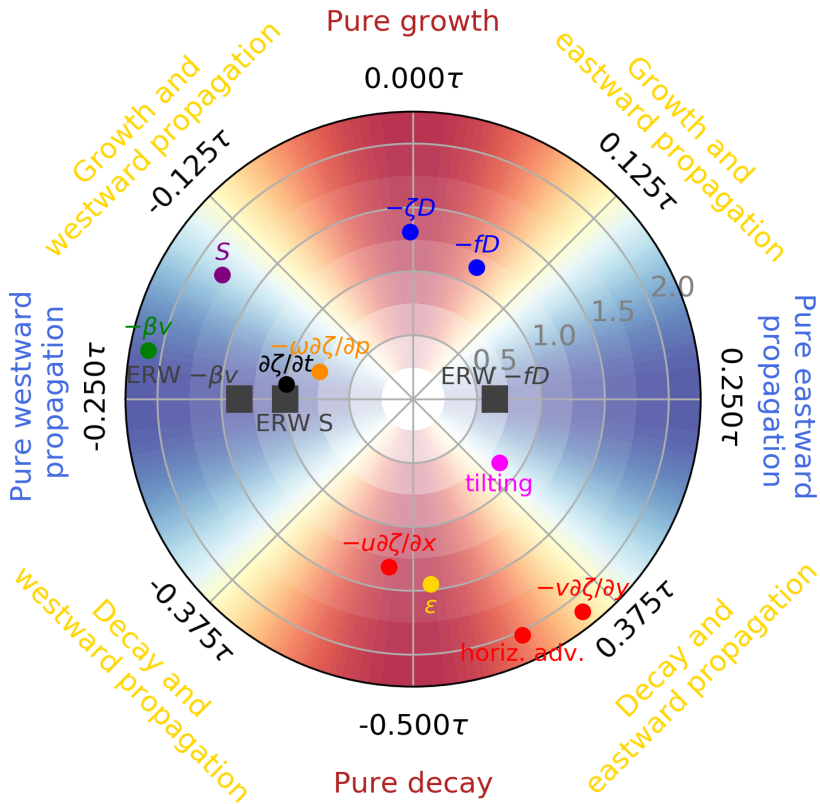


**FIGURE 7** Vorticity budget propagation-growth polar diagram of 850-hPa CCERW vorticity source terms, with normalised RMS amplitude as the radial coordinate, and phase difference  $\theta$  between the source term and the vorticity anomaly, as the azimuthal coordinate. Contrary to regular convention, the azimuthal coordinate axis is zero on the positive vertical axis, and increases in a clockwise direction. This enables growth to be toward the top of the diagram, decay to the bottom, westward propagation to the left, and eastward propagation to the right. The two individual source terms ( $-\beta v$  and  $-fD$ ) and the total source term ( $S$ ) for a theoretical equatorial Rossby wave are shown by the large grey squares.